High-performance, flexible thermoelectric generator based on bulk materials

Cell Reports
Physical Science

CellPress
OPEN ACCESS

Article

High-performance, flexible thermoelectric generator based on bulk materials

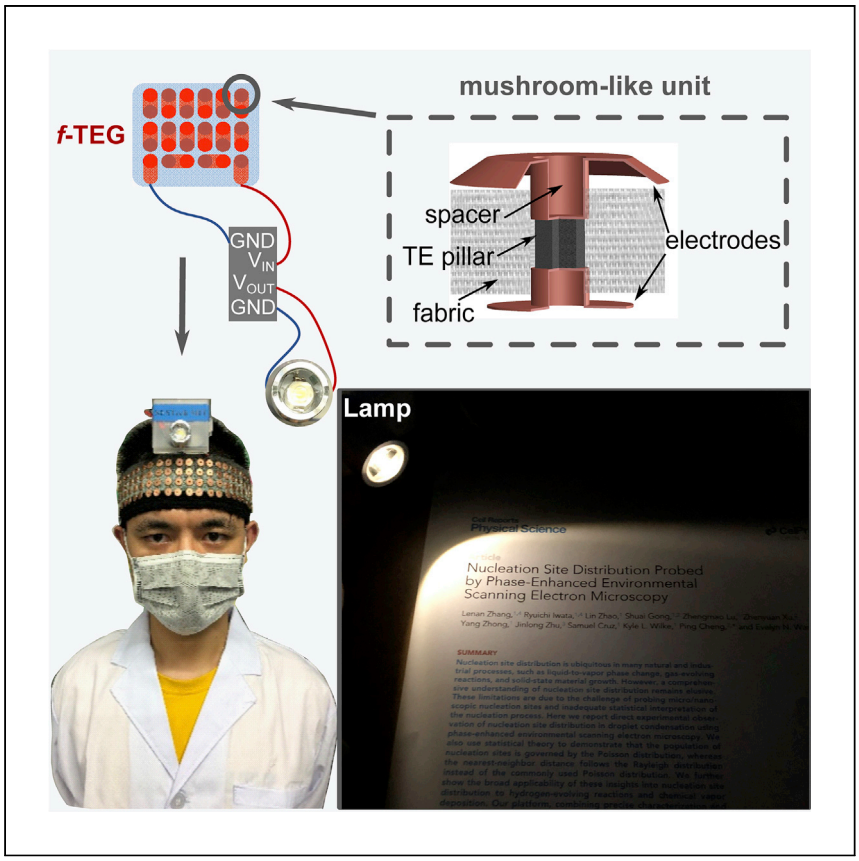

Xu et al. report an *f*-TEG featuring a mushroom-like structure that achieves high output power density on human skin without external heat sink via thermal design. The work provides an example of the design process of *f*-TEGs and paves the pathway toward scalable fabrication of low-cost and high-performance *f*-TEGs.

Qian Xu, Biao Deng, Lenan Zhang, ..., Xinbo Zhang, Gang Chen, Weishu Liu

ritaqxu@mit.edu (Q.X.)
gchen2@mit.edu (G.C.)
liuws@sustech.edu.cn (W.L.)

Highlights

A mushroom-like *f*-TEG achieves high output power density on human skin

The copper electrodes also serve as heat concentrators and spreaders and spacers

An analytical model is developed to predict an *f*-TEG's energy-harvesting performance

Xu et al., Cell Reports Physical Science 3, 100780
March 16, 2022
https://doi.org/10.1016/j.xcrp.2022.100780

Please cite this article in press as: Xu et al., High-performance, flexible thermoelectric generator based on bulk materials, Cell Reports Physical Science (2022), https://doi.org/10.1016/j.xcrp.2022.100780

Cell Reports
Physical Science

CellPress
OPEN ACCESS

Article

High-performance, flexible thermoelectric generator based on bulk materials

Qian Xu,[1,3,*] Biao Deng,[2] Lenan Zhang,[1] Shaoting Lin,[1] Zhijia Han,[2] Qing Zhou,[2] Jun Li,[2] Yongbin Zhu,[2] Feng Jiang,[2] Qikai Li,[2] Pengxiang Zhang,[2] Xinbo Zhang,[2] Gang Chen,[1,*] and Weishu Liu[2,*]

SUMMARY

Flexible thermoelectric generators (*f*-TEGs) are promising solutions to power supply for wearable devices. However, the high fabrication costs and low output power density of conventional *f*-TEGs limit their applications. Here, we present a bulk-material-based *f*-TEG featuring multifunctional copper electrodes for heat concentration and dissipation and fabrics for comfort and heat-leakage reduction. When worn on the forehead, our *f*-TEG's maximum output power density (based on the device's area) reaches 48 $\mu W/cm^2$ at a wind speed of 2 m/s and an ambient temperature of 15°C. A light-emitting diode (LED) powered by our *f*-TEG headband with 100 pairs of thermoelectric pillars can illuminate a paper for reading in a dark room at 17.5°C without an external heat sink or forced convection at the cold side. This work provides a general design approach for high-performance *f*-TEGs at a low cost. The device-level perspectives fill the critical knowledge gap between state-of-the-art material innovations and practical thermoelectric applications.

INTRODUCTION

Wearable technologies have seen increasing deployment and are fueling the spread of the Internet of Things (IoT) revolution. Thermoelectric generators (TEGs) that convert temperature differences into electrical energy can provide power to wearable devices and other IoT devices. Conventional thermoelectric generators sandwich thermoelectric pillars between ceramic substrates and are incapable of bending, thus not suitable for wearable devices. Several strategies have been developed to address the inflexibility of conventional TEGs in recent years,[1,2] including, but not limited to, the use of low-dimensional flexible thermoelectric materials;[3–6] organic or hybrid (organic plus inorganic) thermoelectric materials;[7–10] distribution of discrete conventional rigid thermoelectric pillars on a flexible substrate or in a flexible matrix material;[11–16] painting, printing, and deposition of thermoelectric materials onto a flexible substrate or into flexible matrix materials;[17] and architectural solutions using very thin electronic materials.[18,19] However, the resulting flexible TEGs (*f*-TEGs) have not been translated into practical applications, mainly due to the high fabrication costs (many require relatively complex fabrication steps, including curing polymers and patterning parts with optical lithography) and low output power density (from nW/cm^2 to a few $\mu W/cm^2$). Substantial work remains to be done to apply state-of-the-art thermoelectric materials to practical devices for IoT. Given most wearable electronics require a microwatt to milliwatt level of power input, developing *f*-TEGs with higher output power density is indispensable for bringing self-powered devices from concept to reality.

Most research to enhance a thermoelectric system's performance focuses on improving materials' figure of merit zT to get a higher energy conversion efficiency. However, the

[1]Department of Mechanical Engineering, Massachusetts Institute of Technology, Cambridge, MA 02139, USA

[2]Department of Materials Science and Engineering, Southern University and Science and Technology, Shenzhen 518055, P.R. China

[3]Lead contact

*Correspondence: ritaqxu@mit.edu (Q.X.), gchen2@mit.edu (G.C.), liuws@sustech.edu.cn (W.L.)

https://doi.org/10.1016/j.xcrp.2022.100780

Please cite this article in press as: Xu et al., High-performance, flexible thermoelectric generator based on bulk materials, Cell Reports Physical Science (2022), https://doi.org/10.1016/j.xcrp.2022.100780

improvement in the overall performance of a wearable thermoelectric system from enhancing thermoelectric materials' properties is relatively limited, because the thermal resistances in the substrate materials and interfaces (between body and the device and between the device and ambient air) can be more significant than that of thermoelectric pillars, leading to small temperature drop across the thermoelectric materials and low power output. Though the temperature difference between the skin and the ambient air can be up to 10°C–20°C, the temperature difference across the thermoelectric materials that actually generates power is usually 1°C or less, limiting the performance of *f*-TEGs even made of state-of-the-art thermoelectric materials. We can see this by matching the heat flux across the device: when the human metabolic heat on skin (~50 W/m^2)[20] passes through the thermoelectric materials with a fill factor (the ratio of the active thermoelectric material cross-section area to the area of the substrate in contact with the heat source) of 0.25 and can be effectively dissipated at the cold side, from $q = 0.25\kappa_{TE}\Delta T/d = 50$ W/m^2 with the thermal conductivity of the thermoelectric materials $\kappa_{TE} \sim 1$ W/mK and the thickness of the pillars $d \sim 5$ mm for a bulk-material-based *f*-TEG, the temperature difference across the thermoelectric materials ΔT is about 1°C. The assumed 5-mm pillar thickness used for commercial thermoelectric power generation devices is significantly thicker than that $d \sim 1$ mm in thermoelectric cooling devices, increasing the materials cost and device weight. *f*-TEGs based on thin-film, fiber, or low-dimensional thermoelectric materials have an even bigger challenge because of the much smaller thickness *d*, not to mention that the figure of merit of these materials has not yet been conclusively demonstrated to be able to compete against bulk materials. Therefore, we believe it is more fruitful to work on the device design to increase the temperature drop across the thermoelectric materials.

Nonetheless, device research focusing on maximizing power output from human body heat remains scarce. There have been a few studies on utilizing materials (including thermoelectric material itself, contact materials, electrodes, and substrate materials) with better thermal properties,[13,21–23] tuning the fill factor and the geometry of the thermoelectric pillars,[24–33] and adoption of novel configurations of the thermoelectric pillars and heat exchangers.[34–39] Despite theoretical studies that have suggested further improvement based on device-level optimization or heat transfer analysis,[30,32] there is still a lack of effective and economical design that would generally work for wearable thermoelectric devices.

Here, we demonstrate a mushroom-like *f*-TEG using widely available materials (commercial copper foil, n-type BiTeSe, and p-type BiSbTe alloys) and a four-step fabrication process that achieves record-high output power density on human skin without using an external heat sink via thermal design. When worn on the forehead, our *f*-TEG's maximum output power density (based on the device's area) varies from 6.3 μW/cm^2 (at a wind speed of 0.2 m/s and an ambient temperature of 25°C) to 48 μW/cm^2 (at a wind speed of 2 m/s and an ambient temperature of 15°C). A light-emitting diode (LED) powered by our headband *f*-TEG with 100 pairs of thermoelectric units can illuminate a paper for reading in a completely dark room at 17.5°C without an external heat sink or forced convection at the cold side. This work provides an example of the design process of *f*-TEGs and paves the pathway toward scalable fabrication of low-cost and high-performance *f*-TEGs.

RESULTS AND DISCUSSION

Structure of the flexible thermoelectric generator and design principles based on heat transfer analysis

Figures 1A–1C show our design to reduce the parasitic resistances, maximize the temperature difference across the thermoelectric pillars, and achieve flexibility. In

Please cite this article in press as: Xu et al., High-performance, flexible thermoelectric generator based on bulk materials, Cell Reports Physical Science (2022), https://doi.org/10.1016/j.xcrp.2022.100780

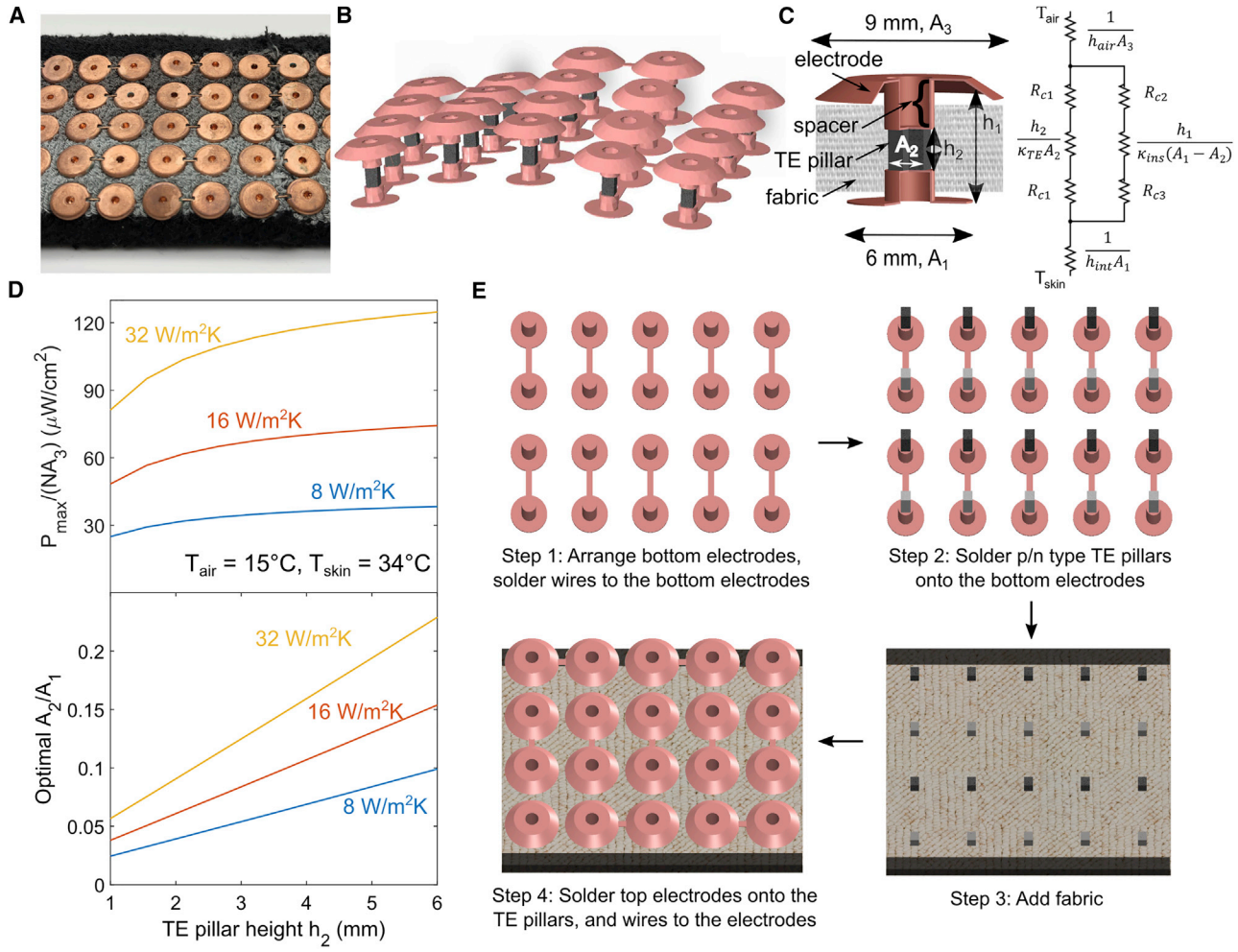

Figure 1. Design and fabrication process for the mushroom-like *f*-TEG

(A) Photo of a section of the wearable headband *f*-TEG. The thermoelectric units are connected by copper wires with a diameter of 0.4 mm.

(B) Schematic illustration of an *f*-TEG network made up of multiple thermoelectric units.

(C) Schematic illustration of the *f*-TEG unit's mushroom-like structure and the thermal resistance circuit (see Figure S8 and Table S1 for a more detailed version). A_1, A_2, and A_3 represent the areas. h_1 and h_2 represent the heights. R_{c1}, R_{c2}, and R_{c3} represent the contact thermal resistances. T_{air} and T_{skin} are the cold-side and the hot-side temperatures. H_{air} is the heat transfer coefficient of the ambient air, and h_{int} is the effective heat transfer coefficient at the contact between the bottom electrode and the skin. κ_{TE} and κ_{ins} are the thermal conductivities of the thermoelectric pillar and the thermal insulation layer between the top and the bottom electrodes.

(D) Calculated maximum output power density (maximum output power divided by the total area of top electrodes NA_3, where N is the number of units) and optimal area ratio (the cross-section area of the thermoelectric pillar to the area of the bottom electrode) as a function of thermoelectric (TE) pillar height. The bottom electrode is at 34°C. The top electrode is under convection at an external temperature of 15°C. The total thickness of the device h_1 is 6 mm, and the supporting fabric has a thermal conductivity of 0.03 W/mK. Three curves represent cases of different heat transfer coefficients at the cold surface. More details about the analytical model can be found in Note S1.

(E) Sketches of the four-step fabrication process.

previously reported *f*-TEGs, soft materials (in most cases polymers) were often used to replace the ceramic substrates in conventional TEGs. These materials have low thermal conductivity and inhibit heat collection at the body side and heat dissipation at the cold side of the *f*-TEG. In this work, multifunctional copper disks with a U-shape vertical cross-section (Figure 1C) are used on the device's hot and cold sides to resolve the issue: they serve as electrodes, spacers, and heat concentrators and spreaders and impart flexibility to the device. (1) The connecting copper wires (with a diameter of 0.4 mm) and the thin copper disks in contact with the

Please cite this article in press as: Xu et al., High-performance, flexible thermoelectric generator based on bulk materials, Cell Reports Physical Science (2022), https://doi.org/10.1016/j.xcrp.2022.100780

thermoelectric pillars provide a current path and flexibility. (2) Because of copper's high thermal conductivity, it also conducts heat very well in the horizontal planes at the two sides of the device, i.e., it concentrates the body heat to provide the heat flux needed for a large ΔT across the thermoelectric pillars and spreads out heat for convection to the ambient. The top disks are larger (with a diameter of 9 mm) to facilitate heat dissipation at the cold side, while the bottom disks are slightly smaller (with a diameter of 6 mm) to accommodate large bending. (3) The raised part in the center of the copper disks acts as the spacers that increase the thermal resistance of the thermal insulation layer between the top and the bottom electrodes (increase h_1 in the thermal resistance circuit in Figure 1C) and thus reduce parasitic heat conduction loss between the cold and the hot sides. Compared with using longer thermoelectric pillars, this strategy reduces the cost and the weight of the device. Adding the fabric helps eliminate the convection between the top and the bottom electrodes. The fabric can be conveniently made of a commercial headband (Figure S2) with a thermal conductivity ~0.03 W/mK. The low thermal conductivity of the fabric and its loose contact with the rest of the thermoelectric unit reduce the heat flux parallel to the heat flux through thermoelectric pillars. Furthermore, while the *f*-TEG network can stand on its own (Figures 1B and S1) and serve as an excellent energy-harvesting device itself, the fabric supports the network of thermoelectric units and protects the thermoelectric pillars from sudden impacts and can absorb sweat to prevent short circuit and provide added comfort in wearing.

We developed an analytical model based on the thermal resistance circuit in Figure 1C to determine the optimal geometries in Figure 1C (details given in Note S1). Generally, a thicker *f*-TEG and higher thermoelectric pillars (larger h_1 and h_2 in Figure 1C) lead to a bigger temperature difference in the pillars so benefit the output thermoelectric voltage. However, to ensure good wearability and flexibility of the *f*-TEG device, the total thickness of the device h_1 is set to be 6 mm. Using the fixed h_1 of 6 mm and the given thermal environment, Figure 1D shows the maximum output power density (based on the total area of the top electrodes since the distribution density of the units can vary) at the optimal area ratio of the thermoelectric pillar's cross-section to the bottom electrode A_2/A_1 increases with the pillar height h_2. Note that, while the maximum output power density depends on the hot and the cold sides temperatures, the best area ratio A_2/A_1 does not and it is uniquely determined by the total thickness h_1, the thermoelectric pillar height h_2, thermal properties of the materials used in the *f*-TEG, and heat transfer coefficients at the surfaces (results in Figure 1D are at three different levels of heat dissipation at the cold side) when maximizing the output power density in the analytical model. Similarly, if A_2/A_1 is fixed instead of h_2, the optimal thermoelectric pillar height h_2 can be determined analytically (for example, Figure 3). We notice the increase in the maximum output power density is less evident when the pillar height h_2 exceeds 2 mm, while the taller thermoelectric pillars are, the more prone to fracture they might be because of potentially larger bending moment (we will discuss this in Figure 4),[11] in addition to increased materials cost. In this work, we use thermoelectric pillars with the dimensions of 1.9 (height) × 1.55 × 1.55 mm, so the A_2/A_1 area ratio is 0.085 (the optimal value at h_1 = 6 mm, a wind speed of 3 to 4 m/s from our analytical model). The edges of copper electrodes are chamfered to prevent cuts and achieve a more premium look and feel.

The fabrication process based on our design is straightforward. Figure 1E sketches out the main fabrication steps of our *f*-TEG device. (1) The customized bottom copper electrodes with the desired geometry determined by our analytical model are distributed uniformly and soldered together with connecting copper wires. (2) The p/n type thermoelectric pillars are soldered onto the bottom electrodes. (3) The

Please cite this article in press as: Xu et al., High-performance, flexible thermoelectric generator based on bulk materials, Cell Reports Physical Science (2022), https://doi.org/10.1016/j.xcrp.2022.100780

thermoelectric units are embedded in a loose-knit fabric (Figures 1A and S2). (4) The customized top copper electrodes are soldered onto the thermoelectric pillars, and the connecting wires are soldered to the top electrodes. Given all the materials used here are commercially available and the fabrication steps are rather basic, we believe the scalable fabrication of our low-cost and high-performance mushroom-like *f*-TEGs can be readily achieved.

Power generation performance

To test the energy-harvesting performance of our *f*-TEG device, we conduct both indoor and outdoor testing. Figure 2A shows the experimental setup for indoor testing. The wearer is sitting in front of an air chamber with the *f*-TEG on the forehead facing the air outlet. The airflow with tunable temperature and velocity is generated by a fan and a heating and refrigerated circulator with a heat exchanger. The wind speed and the air temperature at the chamber outlet are measured by an anemometer and a thermocouple placed near the outlet. In indoor testing, the typical power generation of the *f*-TEG device consisting of 50 pairs of thermoelectric units when a wearer wears it on the forehead as a function of sweeping current is given in Figures 2B (at a wind speed of 0.2 m/s) and 2C (at a wind speed of 2 m/s). Since the skin temperature varies from person to person (Table S4) so the power generation performance could change with different wearers, in Figure 2D, we show performance testing results with more volunteer wearers (including female and male wearers) and comparison with our analytical prediction. The skin temperature in the model is set to be 34 °C, which is the average hot-side temperature we measured. Good agreement is achieved between our analytical model and the measurements. Our *f*-TEG's measured nominal maximum output power densities (based on the device area) are 6.3 $\mu W/cm^2$ at a wind speed of 0.2 m/s, an ambient temperature of 25°C, and 48 $\mu W/cm^2$ at a wind speed of 2 m/s, an ambient temperature of 15°C. These are the highest reported values for *f*-TEGs on human skin without using an external heat sink (Figure 3D; Table S3).[11–13,40,41] The distribution density of the thermoelectric units can vary to meet different power output density and flexibility needs, and a more compact design leads to an even higher output power density but increased stiffness of the device. The typical distribution density that keeps a good balance between performance and wearability for our headbands shown in Figures 1A, 2A, 2E, and 2G is 100 cm^2 per 50 pairs (Figures S3 and S4). The upper limit of the maximum output power density at the extreme packing density can be calculated based on the total area of top electrodes. In this case, it varies from 10 $\mu W/cm^2$ (v_{air} = 0.2 m/s; T_{air} = 25°C) to 76 $\mu W/cm^2$ (v_{air} = 2 m/s; T_{air} = 15°C).

In outdoor testing, the *f*-TEG headband wearer carries a portable data logger in a backpack (Figure 2E) and walks or runs outdoors. Like in indoor testing, two thermocouples are attached to a top electrode (exposed to the ambient air) and a bottom electrode (in contact with human skin) recording temperatures. The *f*-TEG headband is connected to an external resistance of 1 ohm for impedances matching, and the output voltage is being monitored by the data logger. Figure 2F shows our *f*-TEG headband with 50 pairs of thermoelectric units can generate an output power of up to 1.2 mW during an outdoor jog at night at an outdoor temperature of 25°C (estimated running speed: 2.5 m/s; see Video S1), which is comparable to our indoor results in Figure 2D at T_{air} = 25°C and v_{air} = 2 m/s. We notice in Figure 2F, despite some fluctuations in the power output curve, the average power output increases with time due to better heat dissipation at the cold side of the *f*-TEG and potentially increased metabolic heat at the hot side during running. The airflow against the headband and the contact between the headband and the skin would keep changing due to the motion, which may lead to some uncertainties in the measured data. However, it is certain that both the hot-side temperature and the cold-side temperature

Please cite this article in press as: Xu et al., High-performance, flexible thermoelectric generator based on bulk materials, Cell Reports Physical Science (2022), https://doi.org/10.1016/j.xcrp.2022.100780

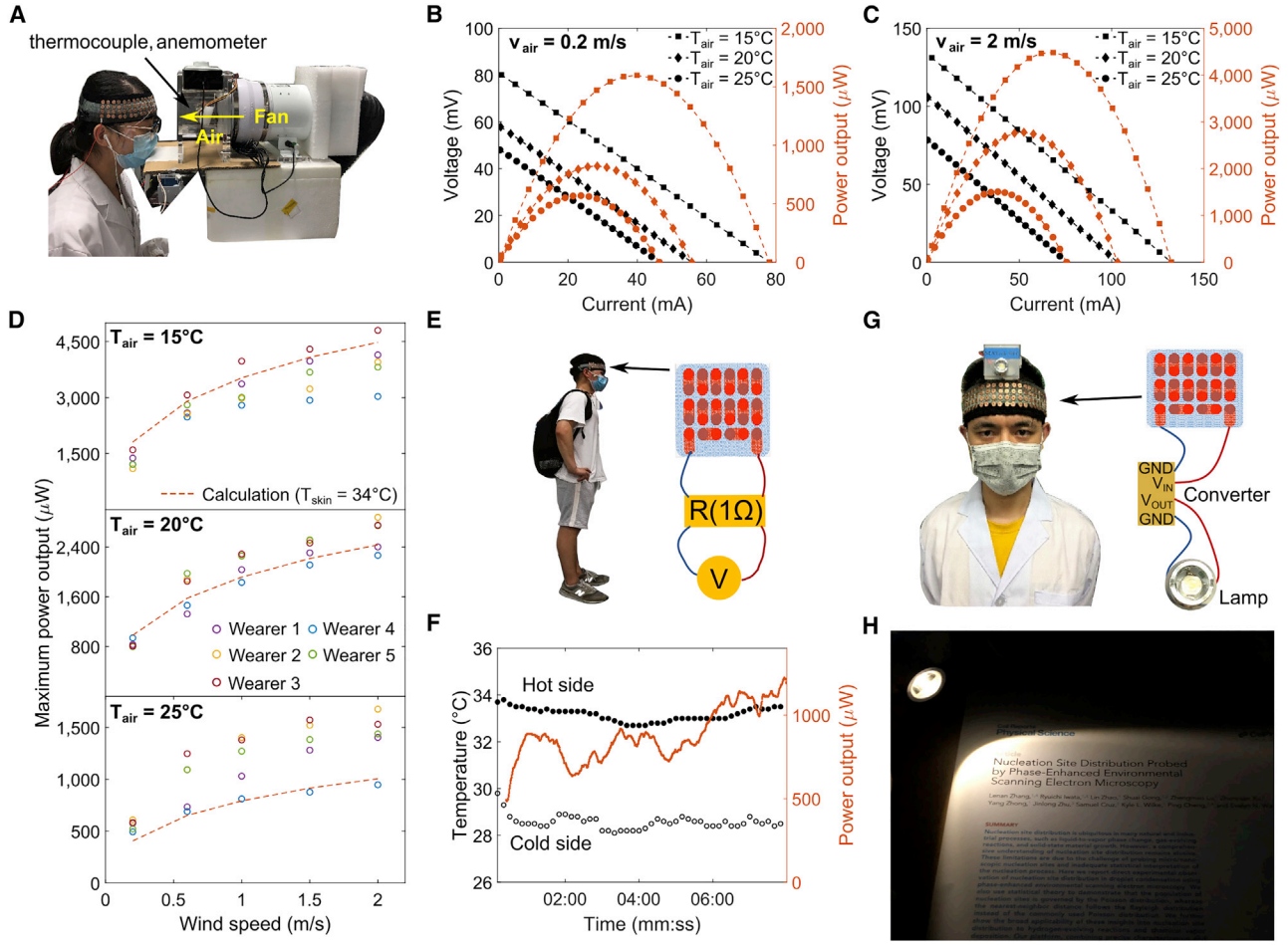

Figure 2. Indoor and outdoor power generation performance

(A) Setup for indoor testing (results shown in B–D) with tunable wind speed and air temperature. The forced air is sourced from a heating and refrigerated circulator (JULABO F25-MA) with a heat exchanger. Fan maximum volume flow rate: 594 m^3/h.

(B and C) Typical power generation curves of the *f*-TEG headband with 50 pairs of p/n thermoelectric units as a function of sweeping current when a wearer wears it on the forehead under various indoor thermal conditions. (B) The wind speed is 0.2 m/s. (C) The wind speed is 2 m/s.

(D) Power generation performance of the *f*-TEG headband with 50 pairs of thermoelectric units as a function of wind speed at 15°C, 20°C, and 25°C in indoor testing: results of five individual measurements and the analytical model. The calculation details can be found in Note S1. The room temperature is 19 °C (tests at T_{air} = 15 °C and 20 °C) and 22 °C (tests at T_{air} = 25 °C).

(E) Setup for outdoor testing (results shown in F): the *f*-TEG headband with 50 pairs of thermoelectric units is connected to a 1 ohm external resistance, and the output voltage is recorded by a portable data logger. Two thermocouples are attached to a top electrode and a bottom electrode in the *f*-TEG, recording temperatures.

(F) Recorded temperatures (left axis) at the hot side (black filled circles) and the cold side (hollow black circles) of the *f*-TEG and output power (right axis, red curve) of the headband during an outdoor jog (average running speed: 2.5 m/s) at night on November 17, 2020 in Shenzhen, China. The outdoor temperature was 25 °C, and there was little wind. See Figure S5 for the same plot with the temperature difference between the hot and the cold sides as the left axis.

(G) A headlamp powered by the *f*-TEG headband: the *f*-TEG is connected to a direct current to direct current (DC-DC) voltage step-up converter (ANALOG DEVICES LTC3108), and the output voltage is boosted to power the LED.

(H) An LED (I-V curve given in Figure S6) is powered by the *f*-TEG headband with 100 pairs of thermoelectric units worn by a seated wearer. The LED can illuminate a paper for reading in a dark room. The room temperature was 17.5 °C, and no forced air was blowing toward the device. Measured output voltage and power were 105 mV, 2.2 mW and 2.5 V, 0.55 mW before and after voltage boost.

decrease at the beginning due to enhanced convection at the top surface, while the hot-side temperature rises later during the exercise. Overall, the output power density aligns with the measured temperature difference between the hot and the cold sides (Figure S5). Besides, we notice in outdoor testing that the fabric also holds up

Please cite this article in press as: Xu et al., High-performance, flexible thermoelectric generator based on bulk materials, Cell Reports Physical Science (2022), https://doi.org/10.1016/j.xcrp.2022.100780

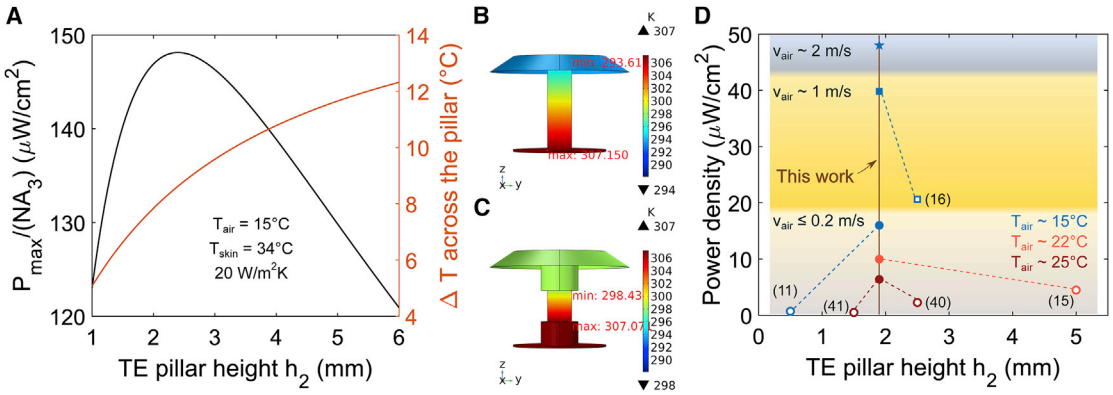

Figure 3. Relation between the maximum output power density of the *f*-TEG and the thermoelectric (TE) pillar height

(A) Calculated maximum output power density (black curve) and temperature difference across the thermoelectric pillar (red curve) as a function of the thermoelectric pillar height h_2 from our analytical model in the ideal case where there is perfect thermal insulation around the thermoelectric pillar between the top and the bottom electrodes. Inputs used in the model are as follows: the total thickness of the device (6 mm); the cross-section of the thermoelectric pillar (1.55 × 1.55 mm); the diameters of the top electrode (9 mm) and the bottom electrode (6 mm); thermal conductivity of the material around the thermoelectric pillar between the top and the bottom electrodes (0 W/mK); the temperatures of the bottom electrode (34 °C) and the top electrode (15 °C); and the heat transfer coefficient at the top surface (20 W/m^{2}K). The calculated temperature difference across the thermoelectric pillar is 8.2 °C at h_2 = 2 mm and 13.2 °C at h_2 = 6 mm.

(B and C) Temperature distribution in the mushroom-like *f*-TEG unit with spacers (C; h_2 = 2 mm) and a similar conventional *f*-TEG unit without spacers (B; h_2 = 5.9 mm) from COMSOL simulations using the same geometry and thermal environment input used in (A). The temperature difference across the thermoelectric pillar in the COMSOL modeling is 13.5 °C (B) and 8.6 °C (C).

(D) A summary of recently developed high-performance *f*-TEGs' output power density based on the total device area (including the space between copper disks). Details of the listed works[11–13,40,41] are given in Table S3.

well against sweat; therefore, we further conduct testing under extreme conditions by thoroughly wetting the headband to demonstrate the robustness of our *f*-TEG device (Figure S7). No short circuit is observed at the drenched state, and the device has an even higher power output at wet states than at the dry state.

To give a more intuitive demonstration of our device's power generation capability, Figures 2G and 2F show that our *f*-TEG headband can power a commercial LED to illuminate a paper for reading in a completely dark room at 17.5°C without an external heat sink or forced convection at the cold side of the *f*-TEG. Hence, we think our *f*-TEG can be readily integrated with commercial headlamps to light the way for outdoor activities like running, hiking, and camping at night. Moreover, given many IoT sensors require less power than LEDs (LEDs usually demand a milliwatt-level power input), we believe our *f*-TEG has even more promising IoT applications.

Comparison with conventional flexible thermoelectric generators

To better elucidate the significance of the thermal design for the enhancement of *f*-TEG power generation performance, we quantitatively compare the maximum output power density and the temperature difference across the thermoelectric pillar between the *f*-TEGs with (our mushroom-like design) and without spacers (conventional design with longer pillars) by using both the analytical model and COMSOL simulations.

In Figures 3A–3C, the total thickness of the device is fixed (6 mm), the bottom electrode is at 34°C, and the upper surface of the top electrode is under convection at an external temperature of 15°C and a heat transfer coefficient of 20 W/m^{2}K (roughly equivalent to the condition when the wind speed is 2 to 3 m/s). An ideal case with negligible thermal contact resistances at the interfaces and perfect insulation around the thermoelectric

Please cite this article in press as: Xu et al., High-performance, flexible thermoelectric generator based on bulk materials, Cell Reports Physical Science (2022), https://doi.org/10.1016/j.xcrp.2022.100780

pillar between the two electrodes is studied to obtain the theoretical maximum values when the materials of insulation layer and adhesives are ultimately optimized. The calculated temperature difference across the thermoelectric pillar (ΔT = 8.2°C at h_2 = 2 mm and ΔT = 13.2°C at h_2 = 6 mm, from the same analytical model used in Figures 1D and 2D) matches the COMSOL simulation results (ΔT = 8.6°C in Figure 3A and ΔT = 13.5°C in Figure 3B). Though a larger temperature difference can be obtained with increasing h_2, the maximum output power density does not necessarily increase with h_2 when the areas of thermoelectric pillar cross-section and electrodes are set. According to Figure 3A, our mushroom-like design with spacers (h_2 = 2 mm; Figure 3B) has a higher maximum output power density than the design without spacers (h_2 = 5.9 mm; Figure 3A) in the ideal case. These findings explain why our mushroom-like *f*-TEG exceeds previously reported *f*-TEGs in terms of output power density based on the total device area (including the space between copper disks) on human skin without using an external heat sink (Figure 3D; Table S3)[11–13,40,41] and reduces cost and weight of thermoelectric materials at the same time.

We further study the mechanical performance of the *f*-TEGs during use by simulating the thermoelectric units (h_2 = 2 mm with spacers and h_2 = 5.9 mm without spacers, with the same total unit thickness and areas of the top and the bottom electrodes) in both shear mode and off-axis compression mode. Conventional Bi_2Te_3-based thermoelectric materials are known to have poor mechanical properties and are subject to fracture. It has been observed that Bi_2Te_3 easily cleaves along the (*00L*) plane.[42,43] A previous density functional theory study has found that the weak van der Waals interactions between the Te1 atoms dominate the failure process of crystalline Bi_2Te_3, leading to a very low ideal shear strength of 0.19 GPa[44] that is only 0.4%–2% of its bulk Young's modulus (10–50 GPa). In reality, the mechanical weak point in the TEGs is the bonding interface between the metallization layer (nickel) and the thermoelectric material (typical bonding strength 10–30 MPa).[45] To quantitatively evaluate the mechanical robustness of the *f*-TEGs, in Figures 4A and 4C, we simulate the maximum shear stress (half of the difference between the maximum and the minimum principal stresses σ_1 and σ_3) in the thermoelectric pillar as a function of the force applied to one side of the chamfered edge of the top electrode along the Z direction (compression mode) and the X+ direction (shear mode) with the bottom electrode being fixed in COMSOL. The colormaps of the displacement field shown in the insets confirm that most of the elastic deformation in the unit happens in the copper electrodes. According to Figures 4B, 4C, 4F, and 4G, the largest maximum shear stress in the pillar occurs near the top and the bottom edges, which can be attributed to the geometry discontinuity between the electrodes and the thermoelectric pillar that causes a local increase of stress. It is in accord with our observation that most failure happens near the contacts in experiments (the nickel layer detaches from the thermoelectric material). In the off-axis compression mode (force applied along the Z direction; Figure 4A), the maximum shear stress in the shorter thermoelectric pillar (with spacers) is always smaller than that in the taller thermoelectric pillar (without spacers). The distribution of the maximum shear stress along one side edge (the red axis outlined in Figures 4B and 4C) in Figure 4D shows the stress concentration near the top edges is more considerable in the conventional design using a taller thermoelectric pillar than our design with spacers in the compression mode. However, when the pillar is subject to shear (force applied along the X+ direction; Figures 4E–4H), more severe stress concentration is observed near the bottom edges of the thermoelectric pillar in the mushroom-like structure than in the design with a taller thermoelectric pillar. The above analysis implies that, compared with the conventional approach, the mushroom-like structure we proposed (at the same total thickness) is beneficial to the device's strength under compression, but not so in the shear mode. There is room for further improvement in the *f*-TEG's mechanical performance,

Please cite this article in press as: Xu et al., High-performance, flexible thermoelectric generator based on bulk materials, Cell Reports Physical Science (2022), https://doi.org/10.1016/j.xcrp.2022.100780

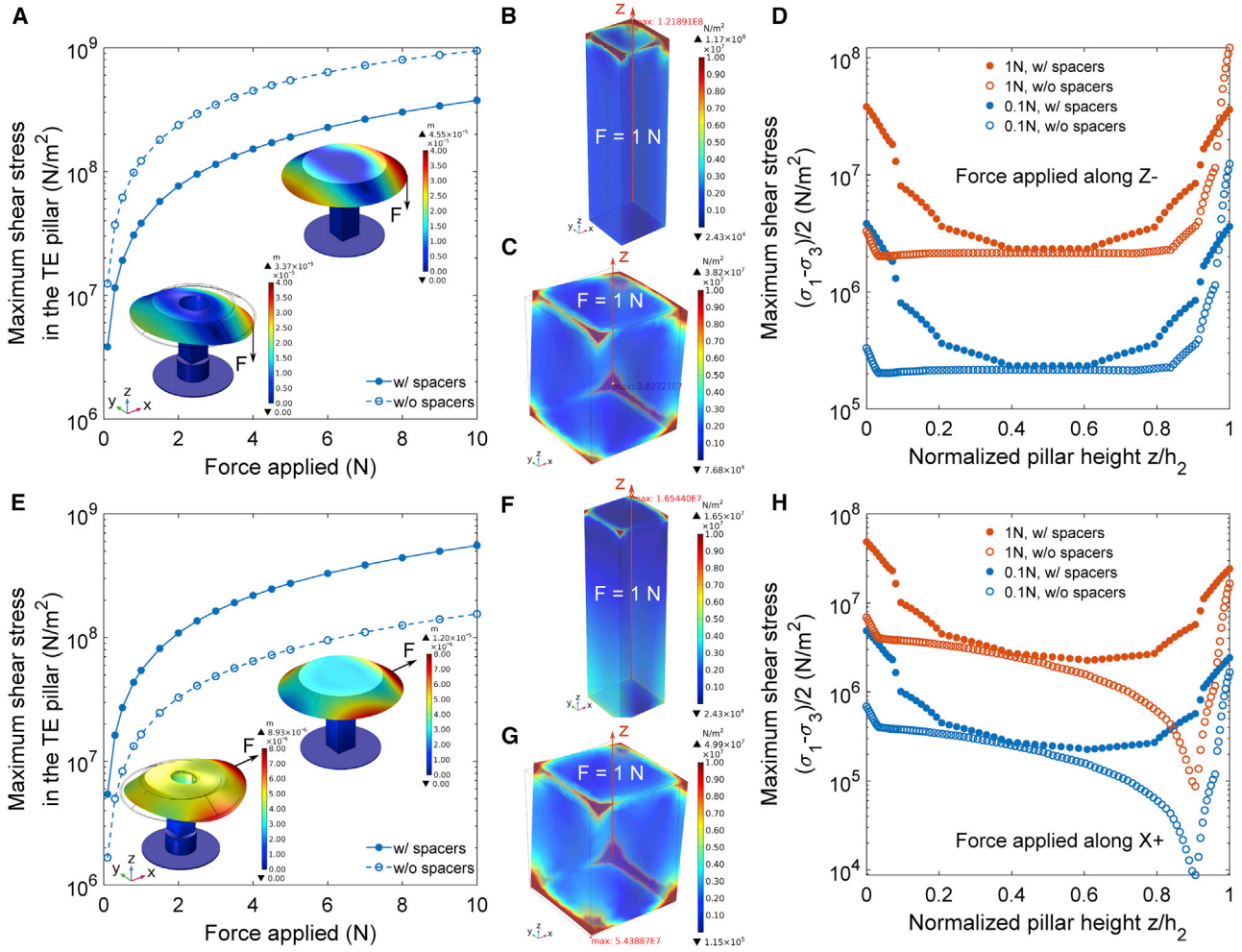

Figure 4. The maximum shear stress in the mushroom-like *f*-TEG with spacers and a similar *f*-TEG of the same thickness without spacers subjected to compression and shear

(A and E) The maximum shear stress in the thermoelectric pillar as a function of the force applied along the Z direction (A; the compression mode) and the X+ direction (E; the shear mode) from COMSOL simulations. Insets: an external force F is applied to the top electrode of the *f*-TEG unit (left: mushroom-like *f*-TEG unit with spacers, the thermoelectric pillar height is 2 mm; right: conventional design without spacers, the thermoelectric pillar height is 5.9 mm). The two units share the same total thickness (6 mm), cross-section of thermoelectric pillar (1.55 × 1.55 mm), and thickness (100 μm) and diameters of top electrode (9 mm) and bottom electrode (6 mm). The colormaps indicate the displacement field at F = 1 N. The principal stresses are the eigenvalues of the stress tensor, computed from the eigenvalue equation, and are ordered so that $\sigma_1 \geq \sigma_2 \geq \sigma_3$.

(B, C, F, and G) Colormaps of the calculated maximum shear stress when a 1 N force is applied at the top electrode in the Z− (B and C) or X+ (F and G) direction and the bottom electrode is fixed. The red "max" marks the maximum shear stress in the thermoelectric pillar in the *f*-TEGs with (C and G) and without spacers (B and F). See Table S2 for more simulation details.

(D and H) Distribution of the maximum shear stress along the red axis outlined in (B), (C), (F), and (G) when F = 0.1 N (blue circles) and F = 1 N (red circles). (D) The force is applied in the Z− direction. (H) The force is applied in the X+ direction.

as we can optimize the shape of the copper spacers and the contacts between the electrodes and the thermoelectric pillar to reduce the stress concentration (e.g., include gradual transitions and chamfer the sharp corners of the pillars). Experimentally, we have measured the electrical resistance of an *f*-TEG with 50 pairs of TE pillars before and after bending. The bending test setup is shown in Video S2, and the normalized resistance against bending radius and bending cycles is given in Figure S10. The results show that the resistance of the *f*-TEG stays the same after 10,000 times of bending, which indicates the device should be able to sustain more than 10,000 times of wear.

In summary, we demonstrate strategies to achieve a higher performance, body-powered *f*-TEG. We use multifunctional thin copper disks as electrodes, heat concentrators and spreaders, spacers, and flexibility enablers. Copper spacers and fabrics are used to suppress the heat loss between the hot and the cold sides through conduction and convection and provide good wearability and comfort even in sweating conditions. We develop an analytical model that predicts an *f*-TEG's energy-harvesting performance and helps determine the optimal geometries of the thermoelectric unit in a given thermal environment. In contrast to most reported *f*-TEGs using thicker thermoelectric pillars to get a larger temperature difference across the pillars (so a larger thermoelectric voltage), our mushroom-like *f*-TEG's performance stands out despite the small thickness of thermoelectric pillars (1.9 mm), reducing weight and cost of thermoelectric materials. In indoor testing, our *f*-TEG's maximum output power density (based on the device area) on human skin reaches 16 $\mu W/cm^2$ at the ambient temperature of 15°C when there is little wind (v_{air} = 0.2 m/s), and the output power density goes up to 48 $\mu W/cm^2$ when the wind speed is increased to 2 m/s. An LED powered by our *f*-TEG headband with 100 pairs of thermoelectric units can illuminate a paper for reading in a completely dark room at 17.5°C without an external heat sink or forced air convection at the cold side. Our *f*-TEG headband with 50 pairs of thermoelectric units can generate 1.2 mW power during a jog at the ambient temperature of 25°C (little wind and running at a speed of 2.5 m/s) in outdoor testing. Our device-level perspectives are critical to bridging state-of-the-art material research and practical thermoelectric applications. Although this paper focuses on power generation, such devices can also be used for personalized cooling. We envision our low-cost and high-performance *f*-TEG would offer an even wider prospect for low-power monitors or control systems in the domains of healthcare, agriculture, transportation, industrial automation, and many more.

EXPERIMENTAL PROCEDURES

Resource availability

Lead contact

Further information and requests for resources should be directed to and will be fulfilled by the lead contact, Qian Xu (ritaqxu@mit.edu).

Materials availability

This study did not generate new unique materials.

Data and code availability

The data that support the plots within this paper and other findings of this study are available from the lead contact upon reasonable request.

Characterization of the thermoelectric materials

The composition analysis of the thermoelectric materials (n-type BiTeSe and p-type BiSbTe alloys from Guangdong Fuxin Technology) was carried out using the electronic probe micro-analysis (EPMA, JEOL-JXA-8100). Samples were cut into pieces of 3 × 3 × 13 mm for electrical properties measurements. Seebeck coefficient and electrical resistivity were measured in a helium atmosphere under a pressure of 0.01 MPa from room temperature to 250°C (CTA-3S, Beijing Cryoall Science and Technology). Thermal conductivity (κ) was calculated by $\kappa = DC_p\rho$, where the thermal diffusivity (D) and the specific heat (C_p) were measured by the laser flash method (LFA 467, Netzsch) using samples with the dimensions of 6 × 6 × 1 mm. Density (ρ) was determined by the Archimedean method. The measured thermoelectric properties are given in Figure S9.

Indoor measurement of *f*-TEG headband performance on human skin

The lab setup is shown in Figure 2A. The current sweep, the output voltage, and temperature measurements were programmed using LABVIEW, and data were collected by a Keithley 2450 multimeter, an NI compact DAQ chassis (cDAQ-9185), and NI-9214 temperature input module. Three thermocouples were used to measure the hot-side temperature T_h, the cold-side temperature T_c of the *f*-TEG, and the air temperature T_{air} at the chamber's outlet. An anemometer (Testo 405i) is located ~6 cm away from the chamber's outlet to measure the wind speed. The current-voltage characteristic curve (I-V curve) of the LED in Figure 2H (Figure S6) was generated by a Keithley 2400 multimeter.

Outdoor measurement of *f*-TEG headband performance on human skin

The outdoor setup is shown in Figure 2E. The *f*-TEG headband with 50 pairs of p/n thermoelectric units was connected to a 1 ohm external resistance, and the output voltage was recorded by a portable data logger (FLUKE 3000FC). Two thermocouples were attached to a top electrode and a bottom electrode in the *f*-TEG recording temperatures. The outdoor temperature was read from a digital thermometer (Xiaomi LYWSD02MMC). The running speed was estimated using the total running distance and the running time.

SUPPLEMENTAL INFORMATION

Supplemental information can be found online at https://doi.org/10.1016/j.xcrp.2022.100780.

ACKNOWLEDGMENTS

The authors thank Prof. Evelyn Wang for helpful discussion. This work was supported by the Centers for Mechanical Engineering Research and Education at MIT and SUSTech (W.L. and G.C.). W.L. was supported by the Guangdong Innovation Research Team Project (2016ZT06G587), the Shenzhen Sci-Tech Fund (KYTDPT20181011104007), and the Tencent Foundation through the XPLORER PRIZE.

AUTHOR CONTRIBUTIONS

G.C., W.L., and Q.X. conceived the idea. B.D. and Q.X. designed the experiments, fabricated the devices, and performed the measurements. J.L., F.J., Z.H., Q.L., P.Z., X.Z., and Q.Z. participated in indoor power generation performance tests. Y.Z. and Z.H. characterized the thermoelectric materials. Q.X. carried out the analytical modeling and COMSOL simulations and analyzed and interpreted the data. S.L. analyzed the simulated mechanical performance. Q.X. and L.Z. wrote the manuscript, and all authors reviewed and commented on the manuscript.

DECLARATION OF INTERESTS

The authors declare no competing interests. MIT and SUSTech are co-inventors of a provisional patent being filed related to this work.

Received: September 9, 2021
Revised: January 10, 2022
Accepted: January 26, 2022
Published: February 22, 2022

Please cite this article in press as: Xu et al., High-performance, flexible thermoelectric generator based on bulk materials, Cell Reports Physical Science (2022), https://doi.org/10.1016/j.xcrp.2022.100780

REFERENCES

1. Du, Y., Xu, J., Paul, B., and Eklund, P. (2018). Flexible thermoelectric materials and devices. Appl. Mater. Today *12*, 366–388.
2. Wang, Y., Yang, L., Shi, X., Shi, X., Chen, L., Dargusch, M.S., Zou, J., and Chen, Z. (2019). Flexible thermoelectric materials and generators: challenges and innovations. Adv. Mater. *31*, 1807916.
3. Wan, C., Gu, X., Dang, F., Itoh, T., Wang, Y., Sasaki, H., Kondo, M., Koga, K., Yabuki, K., Snyder, G.J., et al. (2015). Flexible n-type thermoelectric materials by organic intercalation of layered transition metal dichalcogenide TiS_2. Nat. Mater. *14*, 622–627.
4. Wan, C., Tian, R., Azizi, A.B., Huang, Y., Wei, Q., Sasai, R., Wasusate, S., Ishida, T., and Koumoto, K. (2016). Flexible thermoelectric foil for wearable energy harvesting. Nano Energy *30*, 840–845.
5. Dun, C., Hewitt, C.A., Li, Q., Xu, J., Schall, D.C., Lee, H., Jiang, Q., and Carroll, D.L. (2017). 2D chalcogenide nanoplate Assemblies for thermoelectric applications. Adv. Mater. *29*, 1700070.
6. Kanahashi, K., Pu, J., and Takenobu, T. (2020). 2D materials for large-area flexible thermoelectric devices. Adv. Energy Mater. *10*, 1902842.
7. Yu, C., Murali, A., Choi, K., and Ryu, Y. (2012). Air-stable fabric thermoelectric modules made of N- and P-type carbon nanotubes. Energy Environ. Sci. *5*, 9481–9486.
8. Chen, Y., Zhao, Y., and Liang, Z. (2015). Solution processed organic thermoelectrics: towards flexible thermoelectric modules. Energy Environ. Sci. *8*, 401–422.
9. Kroon, R., Mengistie, D.A., Kiefer, D., Hynynen, J., Ryan, J.D., Yu, L., and Müller, C. (2016). Thermoelectric plastics: from design to synthesis, processing and structure-property relationships. Chem. Soc. Rev. *45*, 6147–6164.
10. Wang, L., Zhang, Z., Geng, L., Yuan, T., Liu, Y., Guo, J., Fang, L., Qiu, J., and Wang, S. (2018). Solution-printable fullerene/TiS_2 organic/inorganic hybrids for high-performance flexible n-type thermoelectrics. Energy Environ. Sci. *11*, 1307–1317.
11. Hong, S., Gu, Y., Seo, J.K., Wang, J., Liu, P., Shirley Meng, Y., Xu, S., and Chen, R. (2019). Wearable thermoelectrics for personalized thermoregulation. Sci. Adv. *5*, eaaw0536.
12. Kim, S.J., We, J.H., and Cho, B.J. (2014). A wearable thermoelectric generator fabricated on a glass fabric. Energy Environ. Sci. *7*, 1959–1965.
13. Liu, Y., Yin, L., Zhang, W., Wang, J., Hou, S., Wu, Z., Zhang, Z., Chen, C., Li, X., Ji, H., et al. (2021). A wearable real-time power supply with a Mg_3Bi_2-based thermoelectric module. Cell Rep. Phys. Sci. *2*, 100412.
14. Kim, M.K., Kim, M.S., Lee, S., Kim, C., and Kim, Y.J. (2014). Wearable thermoelectric generator for harvesting human body heat energy. Smart Mater. Struct. *23*, 105002.
15. Kim, C.S., Yang, H.M., Lee, J., Lee, G.S., Choi, H., Kim, Y.J., Lim, S.H., Cho, S.H., and Cho, B.J. (2018). Self-powered wearable electrocardiography using a wearable thermoelectric power generator. ACS Energy Lett. *3*, 501–507.
16. Wang, Y., Shi, Y., Mei, D., and Chen, Z. (2018). Wearable thermoelectric generator to harvest body heat for powering a miniaturized accelerometer. Appl. Energy *215*, 690–698.
17. Allison, L.K., and Andrew, T.L. (2019). A wearable all-fabric thermoelectric generator. Adv. Mater. Technol. *4*, 1800615.
18. Nan, K., Kang, S.D., Li, K., Yu, K.J., Zhu, F., Wang, J., Dunn, A.C., Zhou, C., Xie, Z., Agne, M.T., et al. (2018). Compliant and stretchable thermoelectric coils for energy harvesting in miniature flexible devices. Sci. Adv. *4*, eaau5849.
19. Peng, J., and Jeffrey Snyder, G. (2019). A figure of merit for flexibility. Science. *366*, 690–691.
20. Leonov, V., and Vullers, R.J.M. (2009). Wearable thermoelectric generators for body-powered devices. J. Electron. Mater. *38*, 1491–1498.
21. Ju, Y.S., and Ghoshal, U. (2000). Study of interface effects in thermoelectric microrefrigerators. J. Appl. Phys. *88*, 4135–4139.
22. Yamashita, O. (2011). Effect of interface layer on the cooling performance of a single thermoelement. Appl. Energy *88*, 3022–3029.
23. He, R., Schierning, G., and Nielsch, K. (2018). Thermoelectric devices: a review of devices, architectures, and contact optimization. Adv. Mater. Technol. *3*, 1700256.
24. Hodes, M. (2010). Optimal pellet geometries for thermoelectric power generation. IEEE Trans. Components Packag. Technol. *33*, 307–318.
25. Fateh, H., Baker, C.A., Hall, M.J., and Shi, L. (2014). High fidelity finite difference model for exploring multi-parameter thermoelectric generator design space. Appl. Energy *129*, 373–383.
26. Dongxu, J., Zhongbao, W., Pou, J., Mazzoni, S., Rajoo, S., and Romagnoli, A. (2019). Geometry optimization of thermoelectric modules: simulation and experimental study. Energy Convers. Manag. *195*, 236–243.
27. Huang, Y.X., Wang, X.D., Cheng, C.H., and Lin, D.T.W. (2013). Geometry optimization of thermoelectric coolers using simplified conjugate-gradient method. Energy *59*, 689–697.
28. Min, G., and Rowe, D.M. (1992). Optimisation of thermoelectric module geometry for "waste heat" electric power generation. J. Power Sourc. *38*, 253–259.
29. Kim, F., Kwon, B., Eom, Y., Lee, J.E., Park, S., Jo, S., Park, S.H., Kim, B.S., Im, H.J., Lee, M.H., et al. (2018). 3D printing of shape-conformable thermoelectric materials using all-inorganic Bi_2Te_3-based inks. Nat. Energy *3*, 301–309.
30. Suarez, F., Nozariasbmarz, A., Vashaee, D., and Öztürk, M.C. (2016). Designing thermoelectric generators for self-powered wearable electronics. Energy Environ. Sci. *9*, 2099–2113.
31. Kishore, R.A., Nozariasbmarz, A., Poudel, B., Sanghadasa, M., and Priya, S. (2019). Ultra-high performance wearable thermoelectric coolers with less materials. Nat. Commun. *10*, 1–13.
32. Zhu, K., Deng, B., Zhang, P., Kim, H.S., Jiang, P., and Liu, W. (2020). System efficiency and power: the bridge between the device and system of a thermoelectric power generator. Energy Environ. Sci. *13*, 3514–3526.
33. Zhang, Q., Liao, J., Tang, Y., Gu, M., Ming, C., Qiu, P., Bai, S., Shi, X., Uher, C., and Chen, L. (2017). Realizing a thermoelectric conversion efficiency of 12% in bismuth telluride/skutterudite segmented modules through full-parameter optimization and energy-loss minimized integration. Energy Environ. Sci. *10*, 956–963.
34. Oki, S., and Suzuki, R.O. (2017). Performance simulation of a flat-plate thermoelectric module consisting of square truncated pyramid elements. J. Electron. Mater. *46*, 2691–2696.
35. Ali, H., Sahin, A.Z., and Yilbas, B.S. (2014). Thermodynamic analysis of a thermoelectric power generator in relation to geometric configuration device pins. Energy Convers. Manag. *78*, 634–640.
36. Yilbas, B.S., and Ali, H. (2015). Thermoelectric generator performance analysis: influence of pin tapering on the first and second law efficiencies. Energy Convers. Manag. *100*, 138–146.
37. Shi, Y., Mei, D., Yao, Z., Wang, Y., Liu, H., and Chen, Z. (2015). Nominal power density analysis of thermoelectric pins with non-constant cross sections. Energy Convers. Manag. *97*, 1–6.
38. Fabián-Mijangos, A., Min, G., and Alvarez-Quintana, J. (2017). Enhanced performance thermoelectric module having asymmetrical legs. Energy Convers. Manag. *148*, 1372–1381.
39. Baranowski, L.L., Jeffrey Snyder, G., and Toberer, E.S. (2013). Effective thermal conductivity in thermoelectric materials. J. Appl. Phys. *113*, 204904.
40. Kim, C.S., Lee, G.S., Choi, H., Kim, Y.J., Yang, H.M., Lim, S.H., Lee, S.G., and Cho, B.J. (2018). Structural design of a flexible thermoelectric power generator for wearable applications. Appl. Energy *214*, 131–138.
41. Zhu, P., Shi, C., Wang, Y., Wang, Y., Yu, Y., Wang, Y., Deng, Y., and Xiao, J. (2021). Recyclable, healable, and stretchable high-power thermoelectric generator. Adv. Energy Mater. *11*, 2100920.
42. Francombe, M.H. (1958). Structure-cell data and expansion coefficients of bismuth telluride. Br. J. Appl. Phys. *9*, 415–417.
43. Wiese, J.R., and Muldawer, L. (1960). Lattice constants of Bi_2Te_3-Bi_2Se_3 solid solution alloys. J. Phys. Chem. Sol. *15*, 13–16.
44. Li, G., Aydemir, U., Morozov, S.I., Wood, M., An, Q., Zhai, P., Zhang, Q., Goddard, W.A., and Snyder, G.J. (2017). Superstrengthening Bi_2Te_3 through nanotwinning. Phys. Rev. Lett. *119*, 085501.
45. Liu, W., Wang, H., Wang, L., Wang, X., Joshi, G., Chen, G., and Ren, Z. (2013). Understanding of the contact of nanostructured thermoelectric n-type $Bi_2Te_{2.7}Se_{0.3}$ legs for power generation applications. J. Mater. Chem. A *1*, 13093–13100.

Cell Reports Physical Science, Volume *3*

Supplemental information

High-performance, flexible thermoelectric generator based on bulk materials

Qian Xu, Biao Deng, Lenan Zhang, Shaoting Lin, Zhijia Han, Qing Zhou, Jun Li, Yongbin Zhu, Feng Jiang, Qikai Li, Pengxiang Zhang, Xinbo Zhang, Gang Chen, and Weishu Liu

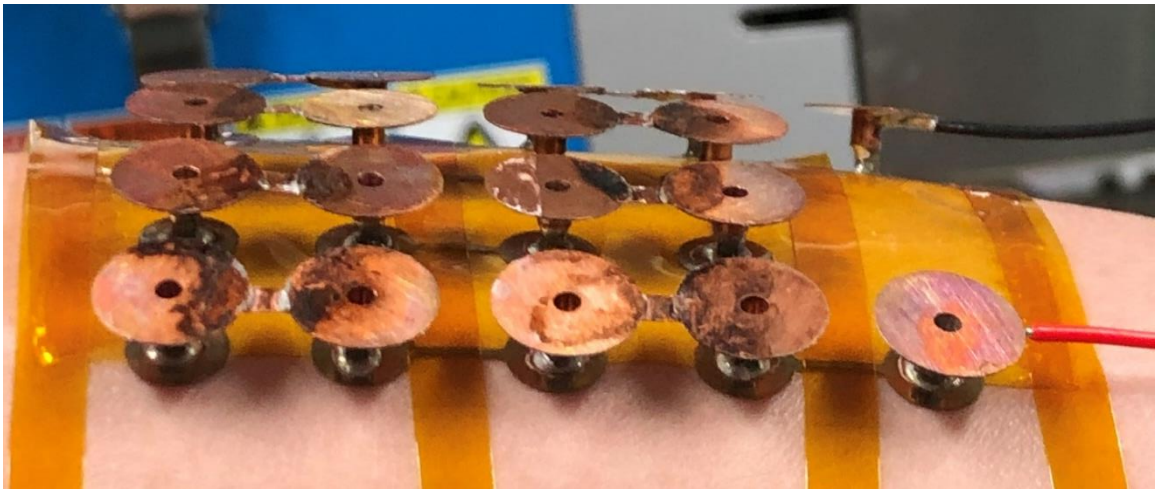

Figure S1. An *f*-TEG network standing on its own without supporting material.

Figure S2. The headband fabric.

The commercial headband (LI-NING 393) is a blending of cotton, polyester fiber, diene elastic fiber and spandex. Thickness: 2.15 mm (natural state), 1.81 mm (tightly compressed).

Figure S3. Demonstration of the *f*-TEG headband's flexibility.

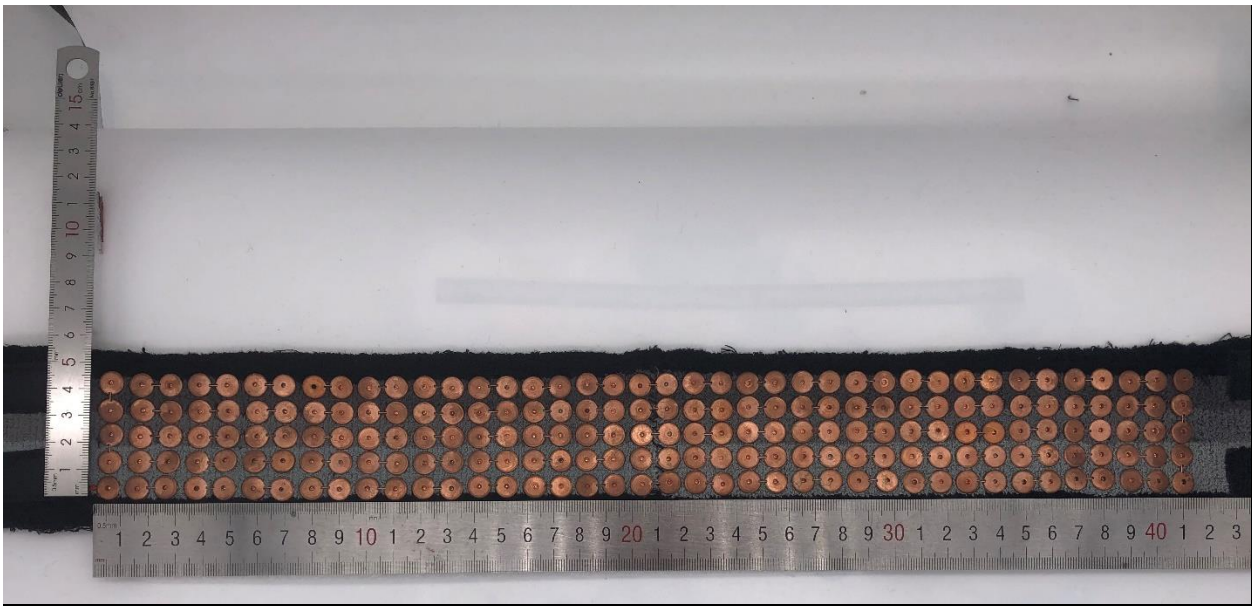

Figure S4. Typical distribution density of the *f*-TEG units.

100 pairs of TE units are distributed evenly in an area of ~ 200 cm^2 (4.8 cm × 41.5 cm).

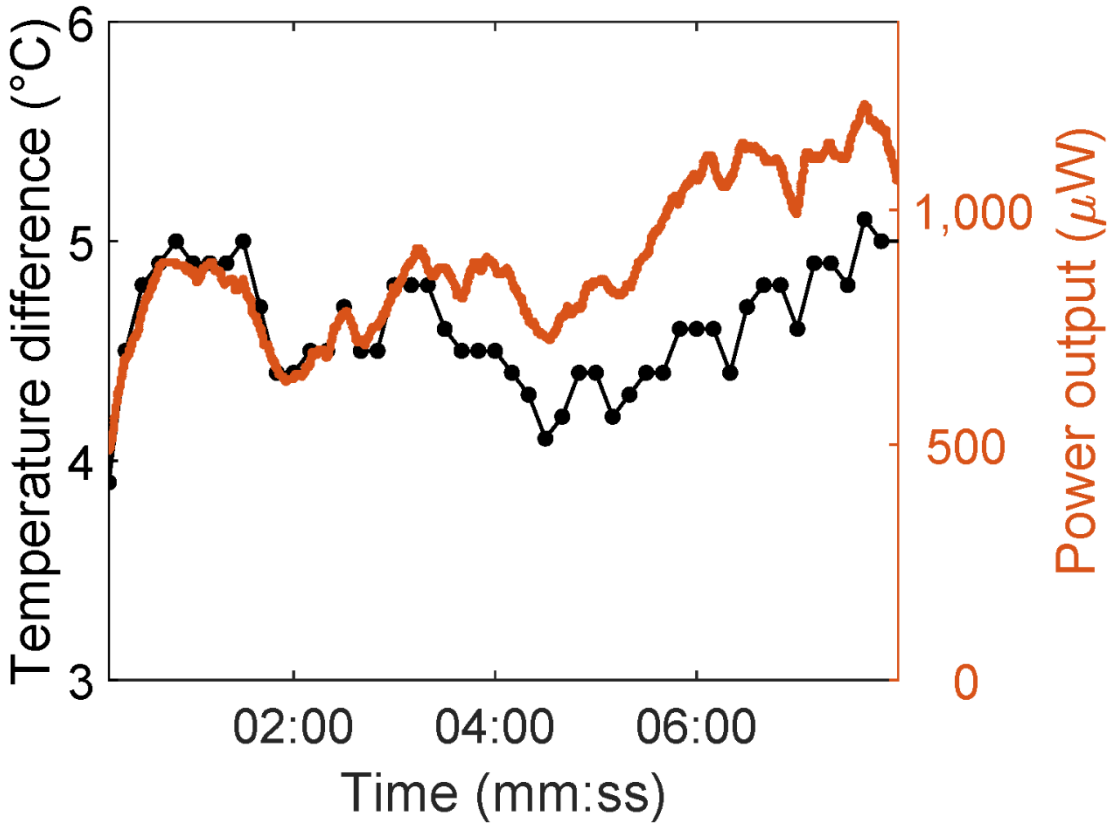

Figure S5. Recorded temperature difference between the hot side and the cold side of the *f*-TEG (left axis, black dots), and output power (right axis, red curve) of the headband in Figure 2F.

The uncertainties in the recorded temperature difference can be due to the change in airflow against the headband and the contact between the headband and the skin caused by motion.

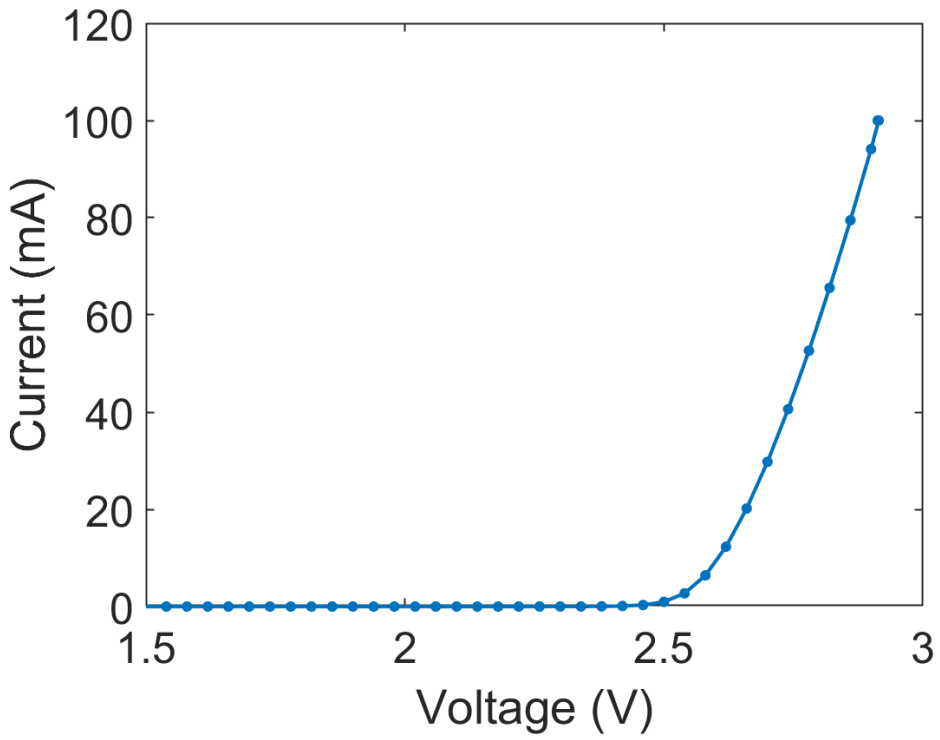

Figure S6. I-V curve of the LED used in Figure 2H.

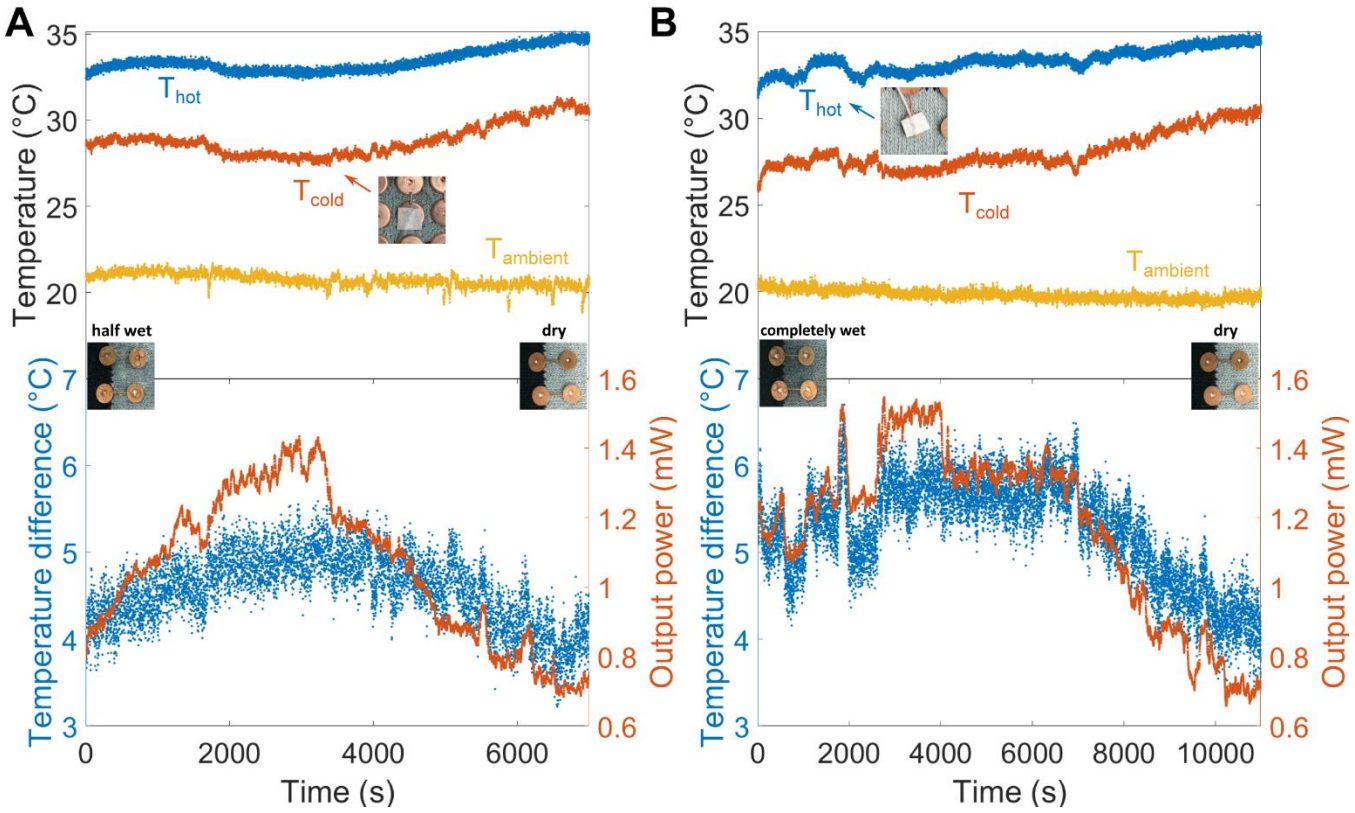

Figure S7. Temperatures at a top electrode and a bottom electrode, and output power of the *f*-TEG headband with 50 pairs of TE units during two drying processes.

(A) from the half wet state to the dry state; (B) from the drenched state to the dry state.

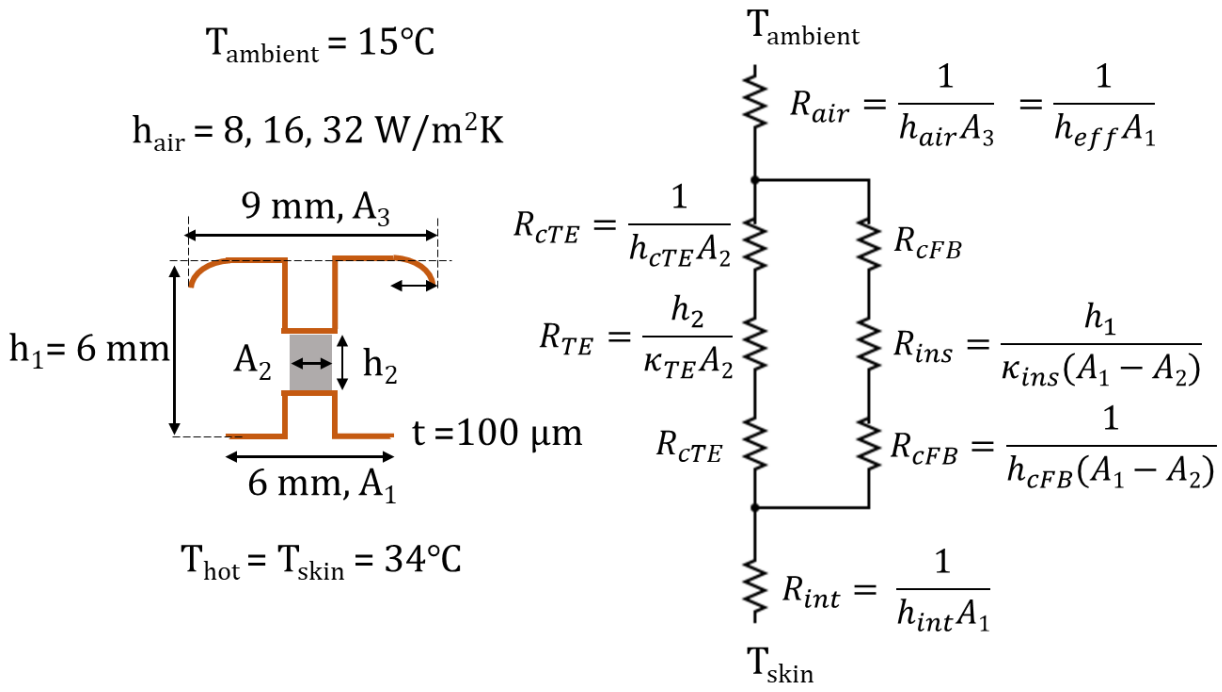

Figure S8. Heat transfer model used in Figure 1D.

A_1, A_2, A_3 represent the areas. h_1, h_2 represent the heights. t is the thickness of the copper electrodes. R_{air}, R_{cTE}, R_{cFB}, R_{int} represent the contact thermal resistances at the top electrode, the top and the bottom surfaces of the TE pillar and the fabric, and between the bottom electrode and the skin. $T_{ambient}$, T_{skin} are the cold side and the hot side temperatures. h_{air} is the heat transfer coefficient of the ambient air and h_{int} is the effective heat transfer coefficient at the contact between the bottom electrode and the skin. κ_{TE} and κ_{ins} are the thermal conductivity of the TE pillar and the thermal insulation layer between the top and the bottom electrodes. Due to the high thermal conductivity of copper, the thermal resistance of the copper disks is neglected and a uniform temperature is assumed in the copper, which can be verified by calculating the characteristic length in the annular fin model $1/\sqrt{\frac{h_{air}}{\kappa_{copper}t}}$ (several centimeters) and COMSOL simulations.

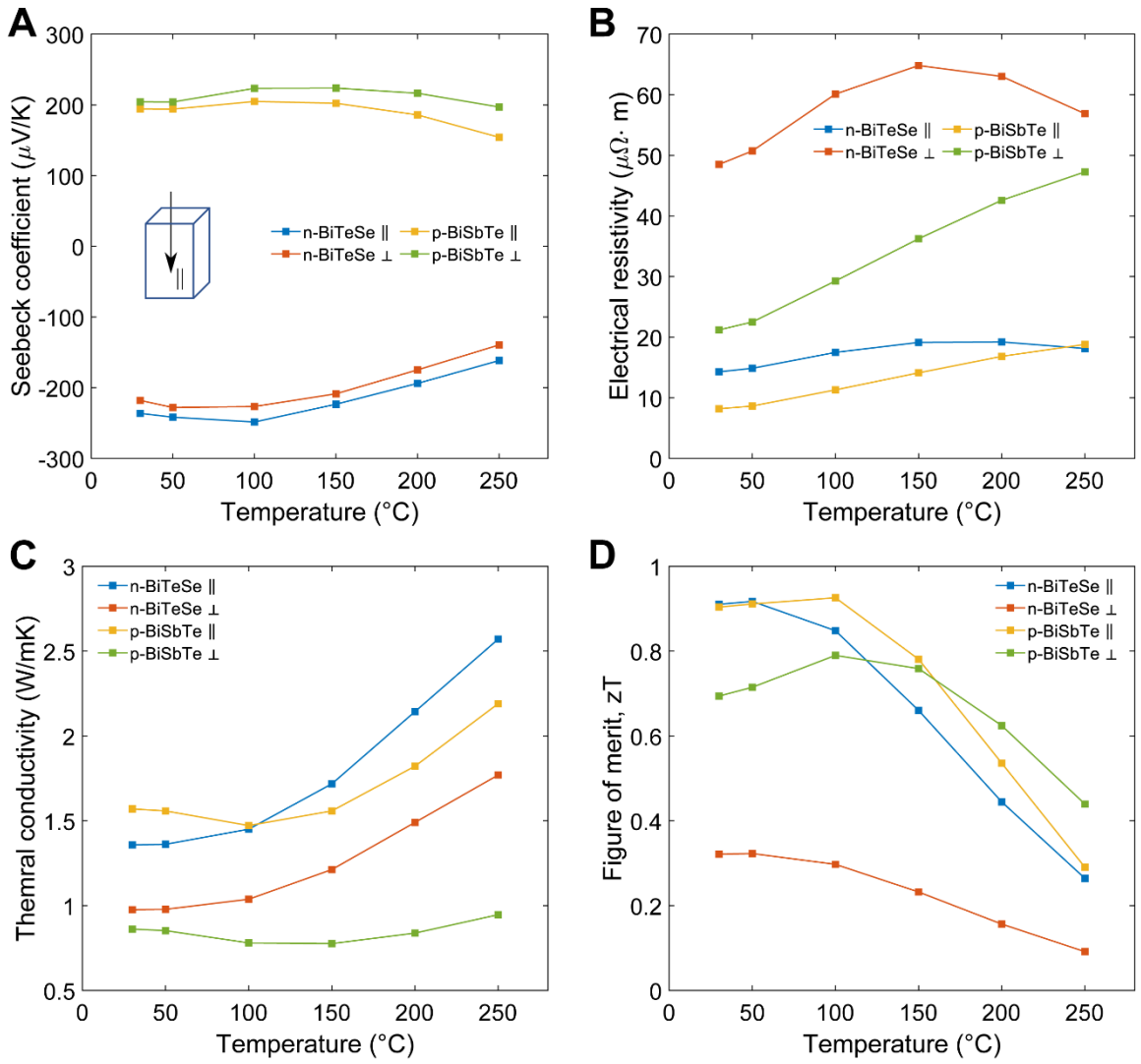

Figure S9. Measured thermoelectric properties of n-type and p-type materials.

(A) Seebeck coefficient; (B) Electrical resistivity; (C) Thermal conductivity; (D) Figure of merit zT.

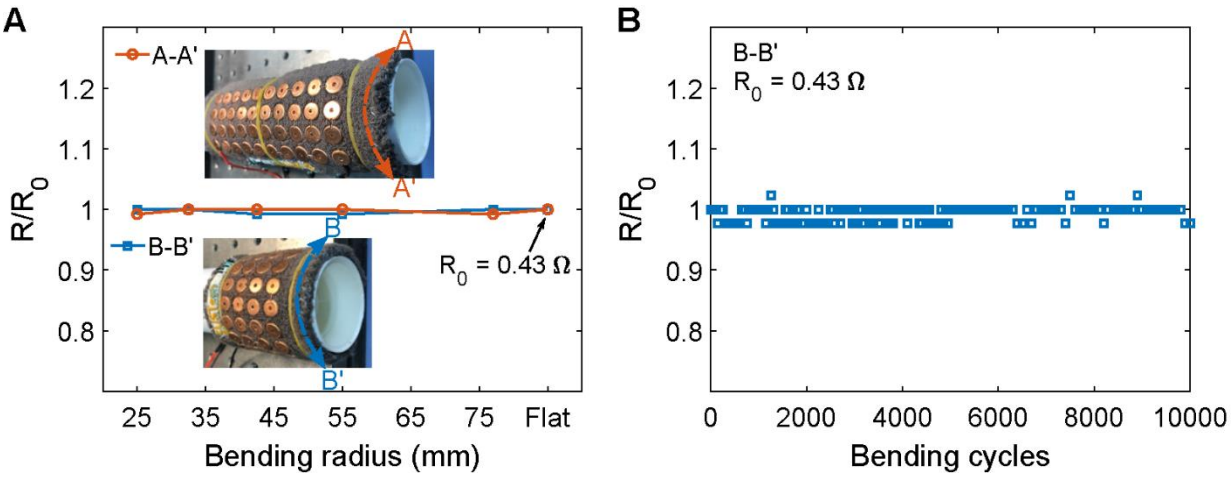

Figure S10. Bending tests of the *f*-TEG headband.

(A) Normalized electrical resistance of the *f*-TEG headband as a function of bending radius along two directions (A-A' and B-B' indicated in the insets); (B) Normalized electrical resistance of the *f*-TEG headband as a function of bending cycles along the B-B' direction (the way of bending when worn on the forehead) with a bending radius of ~31 mm.

Note S1: Analytical Model

From Figure S8, the heat flow Q across the TEG is:

$$Q = \frac{T_{hot} - T_{ambient}}{(R_{air} + R_{int} + \frac{1}{\frac{1}{2R_{cTE} + R_{TE}} + \frac{1}{2R_{cFB} + R_{ins}}})}$$

Temperature difference built up in the TE pillar at steady state ΔT:

$$\Delta T = \frac{QR_{TE}}{(\frac{1}{2R_{cTE} + R_{TE}} + \frac{1}{2R_{cFB} + R_{ins}})(2R_{cTE} + R_{TE})}$$

Maximum output power with specific electrical contact resistance (R_{con}) P_{max}:

$$P_{max} = \frac{(\Delta V)^2}{4R_i} = \frac{(S\Delta T)^2}{4\left(\rho\frac{h_2}{A_2} + R_{con}\right)}$$

Let $\rho'\frac{h_2}{A_2} = \rho\frac{h_2}{A_2} + R_{con}$ and $R'_{air} = R_{air} + R_{int} = \frac{1}{h'_{eff}A_1}$

$$\begin{aligned} P_{max} &= \frac{S^2(T_{hot} - T_{ambient})^2}{4\rho'} \frac{1}{\left(\frac{2R_{cTE} + R_{TE}}{R_{TE}}\right)^2 \left(\frac{R'_{air}}{2R_{cTE} + R_{TE}} + \frac{R'_{air}}{2R_{cFB} + R_{ins}} + 1\right)^2} \frac{A_2}{h_2} \\ &= \frac{S^2(T_{hot} - T_{ambient})^2}{4\rho'} \frac{1}{\left(\frac{R'_{air}}{R_{TE}} + \frac{R'_{air}}{2R_{cFB} + R_{ins}} \cdot \frac{2R_{cTE} + R_{TE}}{R_{TE}} + \frac{2R_{cTE} + R_{TE}}{R_{TE}}\right)^2} \frac{A_2}{h_2} \\ &= \frac{S^2(T_{hot} - T_{ambient})^2}{4\rho'} \frac{1}{\left(\frac{\kappa_{TE}A_2}{h_2h'_{eff}A_1} + \frac{\kappa_{ins}(A_1 - A_2)h_{cFB}(2\kappa_{TE} + h_{cTE}h_2)}{h'_{eff}A_1(2\kappa_{ins} + h_{cFB}h_1)h_{cTE}h_2} + 1 + \frac{2\kappa_{TE}}{h_{cTE}h_2}\right)^2} \frac{A_2}{h_2} \end{aligned}$$

Substitute A_2/A_1 with AR^2, and neglect the electrical contact resistance (R_{con}) for the ideal case:

$$\frac{P_{max}}{A_1} = \frac{S^2(T_{hot} - T_{ambient})^2}{4\rho'} \frac{1}{\left[\frac{\kappa_{TE}AR}{h_2h'_{eff}} + \frac{\kappa_{ins}(1 - AR^2)h_{cFB}(2\kappa_{TE} + h_{cTE}h_2)}{h'_{eff}AR(2\kappa_{ins} + h_{cFB}h_1)h_{cTE}h_2} + \frac{1 + \frac{2\kappa_{TE}}{h_{cTE}h_2}}{AR}\right]^2} \frac{1}{h_2}$$

To maximize $\frac{P_{max}}{A_1}$, minimize the $\left[\frac{\kappa_{TE}AR}{h_2h'_{eff}} + \frac{\kappa_{ins}(1-AR^2)h_{cFB}(2\kappa_{TE}+h_{cTE}h_2)}{h'_{eff}AR(2\kappa_{ins}+h_{cFB}h_1)h_{cTE}h_2} + \frac{1+\frac{2\kappa_{TE}}{h_{cTE}h_2}}{AR}\right]^2$ term by setting the optimal A_2/A_1 to:

$$\frac{A_2}{A_1} = \frac{1 + \frac{2\kappa_{TE}}{h_{cTE}h_2} + \frac{\kappa_{ins}\,h_{cFB}(2\kappa_{TE} + h_{cTE}h_2)}{h'_{eff}(2\kappa_{ins} + h_{cFB}h_1)h_{cTE}h_2}}{\frac{\kappa_{TE}}{h_2h'_{eff}} - \frac{\kappa_{ins}\,h_{cFB}(2\kappa_{TE} + h_{cTE}h_2)}{h'_{eff}(2\kappa_{ins} + h_{cFB}h_1)h_{cTE}h_2}}$$

Heat flux q (based on the area of the bottom electrode) across the TEG is independent of h_2 and h_{cTE}:

$$\frac{Q}{A_1} = q = \frac{T_{hot} - T_{ambient}}{(\frac{1}{h_{eff}} + \frac{1}{\frac{A_2/A_1}{\frac{2}{h_{cTE}} + \frac{h_2}{\kappa_{TE}}} + \frac{1 - A_2/A_1}{\frac{2}{h_{cFB}} + \frac{h_1}{\kappa_{ins}}}})} = \frac{T_{hot} - T_{ambient}}{(\frac{1}{h'_{eff}} + \frac{1}{h'_{eff} + \frac{2}{\frac{2}{h_{cFB}} + \frac{h_1}{k_{ins}}}})}$$

$$\Delta T = \frac{QR_{TE}}{\left(\frac{1}{2R_{cTE}+R_{TE}}+\frac{1}{2R_{cAG}+R_{ins}}\right)(2R_{cTE}+R_{TE})} = \frac{qA_1R_{TE}}{\left(1+\frac{2R_{cTE}+R_{TE}}{2R_{cFB}+R_{ins}}\right)}$$

$$= q\frac{h_2}{\kappa_{TE}\left(\frac{A_2}{A_1}+\frac{\left(1-\frac{A_2}{A_1}\right)\left(2\frac{1}{h_{cTE}}+\frac{h_2}{\kappa_{TE}}\right)}{2\frac{1}{h_{cFB}}+\frac{h_1}{\kappa_{ins}}}\right)}$$

$$= \frac{T_{hot}-T_{ambient}}{\left(\frac{1}{h'_{eff}}+\frac{1}{h'_{eff}+\frac{2}{\frac{2}{h_{cFB}}+\frac{h_1}{k_{ins}}}}\right)}\frac{h_2}{\kappa_{TE}\left(\frac{A_2}{A_1}+\frac{\left(1-\frac{A_2}{A_1}\right)\left(2\frac{1}{h_{cTE}}+\frac{h_2}{\kappa_{TE}}\right)}{2\frac{1}{h_{cFB}}+\frac{h_1}{\kappa_{ins}}}\right)}$$

$$= \frac{T_{hot}-T_{ambient}}{\left(\frac{1}{h'_{eff}}+\frac{1}{h'_{eff}+\frac{2}{\frac{2}{h_{cFB}}+\frac{h_1}{k_{ins}}}}\right)}\cdot\frac{1}{\left(1+\frac{2k_{TE}}{h_2h_{cTE}}\right)\left(h'_{eff}+\frac{2}{\frac{2}{h_{cFB}}+\frac{h_1}{k_{ins}}}\right)}$$

$$= \frac{T_{hot}-T_{ambient}}{\left(\frac{2}{h'_{eff}\left(\frac{2}{h_{cFB}}+\frac{h_1}{k_{ins}}\right)}+2\right)\left(1+\frac{2k_{TE}}{h_2h_{cTE}}\right)}$$

where the physical quantities are summarized in Table S1.

The convective heat transfer coefficient for air flow h_{air} can be approximated to: [1,2]

$$h_{air} = \begin{cases} 14.41\times v^{0.358} & (0.02 < v \le 2\ m/s) \\ 12.12\ -\ 1.16\times v\ +\ 11.6\times v^{0.5} & (2\ \mathrm{m/s} < v < 20\ m/s) \end{cases}$$

where v is the wind speed.

Table S1. Physical quantities used in the heat transfer model in Figure S8.

Physical quantity	Symbol	Value
Hot side temperature of TE module (skin temperature)	T_{hot}	34°C
Ambient temperature	$T_{ambient}$	15°C
Thermal conductivity of the TE pillars (the average of n and p type materials)	κ_{TE}	1.4 W/(m·K)
Thermal conductivity of the insulation layer (the fabric matrix)	κ_{ins}	0.03 W/(m·K) Ideal case: 0 W/(m·K)
Area of a top electrode	A_3	$\pi(9\ mm)^2/4$
Area of a TE pillar's cross-section	A_2	1.55 mm x 1.55 mm
Area of a bottom electrode	A_1	$\pi(6\ mm)^2/4$
Convective heat transfer coefficient of the ambient air	h_{air}	Input variable
Total thickness of the device	h_1	6 mm
TE pillar height	h_2	Input variable
Effective heat transfer coefficient at the cold side considering extended heat dissipation area	h_{eff}	$h_{air}A_3/A_1$
Thermal contact conductance coefficient at the interface between the bottom electrode and human skin	h_{int}	100 W/(m^2·K) Ideal case: 1e9 W/(m^2·K)
Thermal contact resistance between the bottom electrode and human skin	R_{int}	$1/(h_{int}A_1)$
Effective heat transfer coefficient considering extended heat dissipation area and thermal contact resistance R_{int}	h'_{eff}	$1/(1/h_{eff} + 1/h_{int})$
Thermal contact conductance coefficient at the interface between the electrode and the TE pillar	h_{cTE}	4120 W/(m^2·K) Ideal case: 1e9 W/(m^2·K)
Thermal contact conductance coefficient at the interface between the electrode and the fabric	h_{cFB}	1e9 W/(m^2·K)
Thermal resistance in the insulation layer	R_{ins}	$h_1/\kappa_{ins}/(A_1-A_2)$
Thermal resistance in the TE pillar	R_{TE}	$h_2/(\kappa_{TE}A_2)$
Thermal resistance in the air	R_{air}	$1/(h_{air}A_3)$
Thermal contact resistance at the interface between the electrode and the TE pillar	R_{cTE}	$1/(h_{cTE}A_2)$
Thermal contact resistance at the interface between the electrode and the fabric	R_{cFB}	$1/h_{cFB}/(A_1-A_2)$
Internal electrical resistance	R_i	$\rho h_2/A_2$
Seebeck coefficient of the TE pillars (the average of n and p type)	S	205e-6 V/K
Electrical resistivity of the TE pillars (the average of n and p type)	ρ	8.3e-6 Ω m

Table S2. Material properties used in the COMSOL Heat Transfer and Solid Mechanics simulation.

	Bi_2Te_3	Copper
Heat capacity at constant pressure	154 J/(kg·K)	385 J/(kg·K)
Density	7700 kg/m^3	8960 kg/m^3
Thermal conductivity	1.40 W/(m·K)	400 W/(m·K)
Young's modulus	50e9 Pa	110e9 Pa
Poisson's ratio	0.241	0.35

Table S3. A summary of bulk-based wearable *f*-TEGs' output power density P_{max} (based on device area) on the human body without external heat sinks.

TE material	TE pillar dimension	Ambient temperature and wind speed	P_{max} ($\mu W/cm^2$)	Heat source	Ref
Commercial TE alloys (TEC1-07101, Jiangxi Thermonamic Electronics Corp. Ltd.)	5 mm (H) × 1 mm × 1 mm	22°C, natural convection	4.5	human skin (32°C)	3 (15*)
		22°C, v_{air} = 1.4 m/s	10.7		
n: $Bi_{0.5}Sb_{1.5}Te_3$, p: $Bi_2Te_{2.7}Se_{0.3}$	2.5 mm (H) × 1 mm × 1 mm	25°C, natural convection	2.28	artificial arm (33.9°C)	4 (40*)
		25°C, v_{air} = 1 m/s	4.88		
		25°C, v_{air} = 2 m/s	6.2		
n: Bi_2Te_3 p: Sb_2Te_3	0.5 mm (H), ~1.8** mm (diameter)	15°C, outdoor, wind speed not mentioned	~0.75** (an output power of 3 μW)	human skin	5 (11*)
n: Bi_2Te_3 p: Sb_2Te_3	1.5 mm (H) × 1 mm × 1 mm	Room temperature, natural convection	0.516	human skin	6 (41*)
n: $Mg_{3.2}Bi_{1.498}Sb_{0.5}Te_{0.002}$ p: $Bi_{0.4}Sb_{1.6}Te_3$	2.5 mm × 2.5 mm × 2.5 mm	16°C, v_{air} = 1.1 m/s	13.6	human skin	7 (16*)
Commercial BiTeSe (n) and BiSbTe (p) alloys (Guangdong Fuxin Technology Co., Ltd.)	1.9 mm (H) × 1.55 mm × 1.55 mm	25°C, natural convection	6.0	human skin (31~35°C)	This work
		25°C, v_{air} = 0.2 m/s	6.3		
		25°C, v_{air} = 1 m/s	14.2		
		25°C, v_{air} = 2 m/s	16.8		
		22°C, natural convection	9.7		
		22°C, v_{air} = 0.2 m/s	10		
		15°C, v_{air} = 0.2 m/s	16		
		15°C, v_{air} = 1 m/s	39.8		
		15°C, v_{air} = 2 m/s	48		

* Reference number in the manuscript.

** Estimated from a figure with a scale bar because the detailed numbers are not given in the publication.

Table S4. Comparison between skin temperatures at the forehead and at the wrist from thermal camera temperature measurement.

Volunteer	$T_{ambient}$ = 22°C	$T_{ambient}$ = 25°C
Male 1		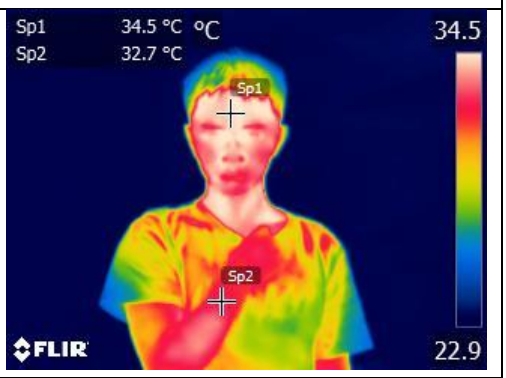
Male 2		
Male 3		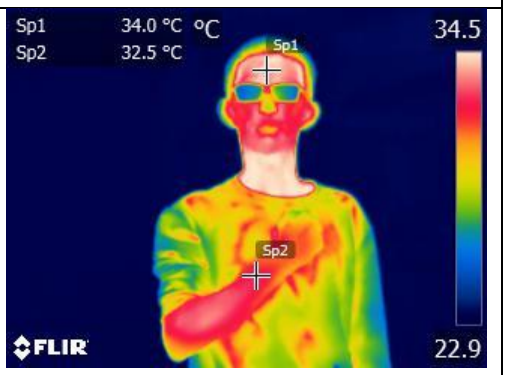
Female 1	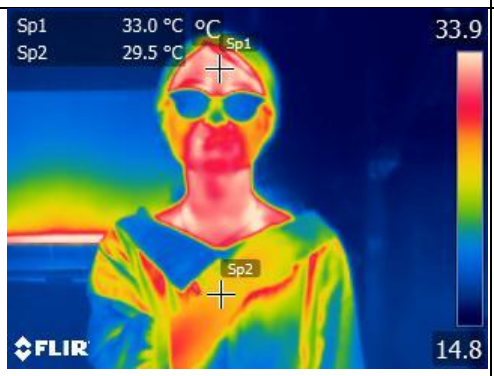	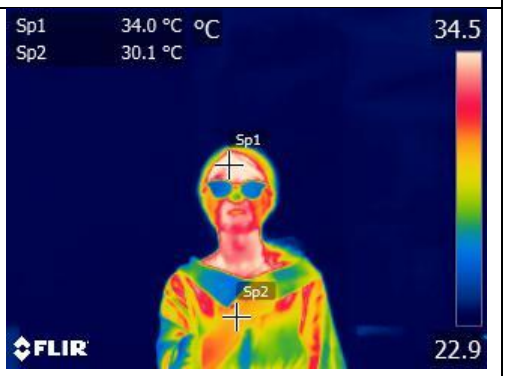
Average	Forehead: 33.33°C Wrist: 29.95°C	Forehead: 34.13°C Wrist: 31.13°C
$T_{25°C, ave}$ - $T_{22°C, ave}$	Forehead: 0.8°C Wrist: 1.8°C	

References:

1. Kurazumi, Y., Tsuchikawa, T., Yamato, Y., Sakoi, T., Bolashikov, Z., Kondo, E., Fukagawa, K., Tobita, K., Matsubara, N., and Horikoshi, T. (2013). Measurement of Heat Transfer Coefficients of Leg-out Sitting and Chair Sitting Human Body under Forced Convection from Front and Back. J. Hum. Living Environ. *20*, 51–61.
2. Convective Heat Transfer https://www.engineeringtoolbox.com/convective-heat-transfer-d_430.html.
3. Hong, S., Gu, Y., Seo, J.K., Wang, J., Liu, P., Shirley Meng, Y., Xu, S., and Chen, R. (2019). Wearable thermoelectrics for personalized thermoregulation. Sci. Adv. *5*, eaaw0536.
4. Kim, C.S., Lee, G.S., Choi, H., Kim, Y.J., Yang, H.M., Lim, S.H., Lee, S.G., and Cho, B.J. (2018). Structural design of a flexible thermoelectric power generator for wearable applications. Appl. Energy *214*, 131–138.
5. Kim, S.J., We, J.H., and Cho, B.J. (2014). A wearable thermoelectric generator fabricated on a glass fabric. Energy Environ. Sci. *7*, 1959–1965.
6. Zhu, P., Shi, C., Wang, Y., Wang, Y., Yu, Y., Wang, Y., Deng, Y., and Xiao, J. (2021). Recyclable, Healable, and Stretchable High-Power Thermoelectric Generator. Adv. Energy Mater., 2100920.
7. Liu, Y., Yin, L., Zhang, W., Wang, J., Hou, S., Wu, Z., Zhang, Z., Chen, C., Li, X., Ji, H., et al. (2021). A wearable real-time power supply with a Mg_3Bi_2-based thermoelectric module. Cell Reports Phys. Sci., 100412.